BNL-211639-2019-JAAM

# Highly Active and Stable Carbon Nanosheets Supported Iron Oxide for Fischer-Tropsch to Olefins Synthesis

Y. Zhou, E. Stavitski

To be published in "ChemCatChem"

March 2019

Photon Sciences

**Brookhaven National Laboratory**

**U.S. Department of Energy**

USDOE Office of Science (SC), Basic Energy Sciences (BES) (SC-22)

Notice: This manuscript has been authored by employees of Brookhaven Science Associates, LLC under Contract No. DE-SC0012704 with the U.S. Department of Energy. The publisher by accepting the manuscript for publication acknowledges that the United States Government retains a non-exclusive, paid-up, irrevocable, world-wide license to publish or reproduce the published form of this manuscript, or allow others to do so, for United States Government purposes.

# DISCLAIMER

This report was prepared as an account of work sponsored by an agency of the United States Government. Neither the United States Government nor any agency thereof, nor any of their employees, nor any of their contractors, subcontractors, or their employees, makes any warranty, express or implied, or assumes any legal liability or responsibility for the accuracy, completeness, or any third party's use or the results of such use of any information, apparatus, product, or process disclosed, or represents that its use would not infringe privately owned rights. Reference herein to any specific commercial product, process, or service by trade name, trademark, manufacturer, or otherwise, does not necessarily constitute or imply its endorsement, recommendation, or favoring by the United States Government or any agency thereof or its contractors or subcontractors. The views and opinions of authors expressed herein do not necessarily state or reflect those of the United States Government or any agency thereof.

# Highly Active and Stable Carbon Nanosheets Supported Iron Oxide for Fischer-Tropsch to Olefins Synthesis

Yunyun Zhou,*[a,b] Sittichai Natesakhawat,[a,c] Thuy-Duong Nguyen-Phan,[a,b] Douglas R. Kauffman,[a] Chris M. Marin,[a,b] Kim Kisslinger,[d] Ruoqian Lin,[d] Huolin L. Xin,[d]** Eli Stavitski,[e] Klaus Attenkofer,[e] Yijie Tang,[f] Yisong Guo,[f] Iradwikanari Waluyo,[e] Amitava Roy,[g] Jonathan W. Lekse,[a] Yang Yu,[a,b]*** John Baltrus,[a] Yu Lu,[a]**** Christopher Matranga,[a] and Congjun Wang*[a,b]

**Abstract:** Light olefins production utilizes the energy intensive process of steam cracking. Fischer-Tropsch to olefins (FTO) synthesis potentially offers a more sustainable alternative. Here we show a promising FTO catalyst comprised of iron oxide nanoparticles supported on carbon nanosheets (CNS) fabricated from the carbonization of potassium citrate, which incorporates well dispersed K-promoter throughout the CNS support. This catalyst exhibits, to the best of our knowledge, the highest iron time yield of 1790–1990 $\mu mol_{CO}/g_{Fe}$•s reported in the literature, 41% light olefins selectivity, and over 100 hours stable activity, making it one of the best performing FTO catalysts. Detailed characterization illustrates that the CNS support facilitates iron oxide reduction to metallic iron, leading to efficient transformation to the active iron carbide phase during FTO reaction. Since K is a commonly used promoter, our K-promoted CNS support potentially has broad utility beyond the FTO reactions demonstrated in the current study.

[a] Dr. Y. Zhou, Dr. S. Natesakhawat, Dr. T-D. N-P., Dr. D. R. Kauffman, Dr. C. M. Marin, Dr. J. W. Lekse, Dr. Y. Yu, Dr. J. Baltrus, Dr. Y. Lu, Dr. C. Matranga, Dr. C. Wang
National Energy Technology Laboratory
Pittsburgh, PA 15236, USA
E-mail: yunyun.zhou@netl.doe.gov, congjun.wang@netl.doe.gov
[b] Dr. Y. Zhou, Dr. T-D. N-P., Dr. C. M. Marin, Dr. Y. Yu, Dr. C. Wang
AECOM
Pittsburgh, PA 15236, USA
[c] Dr. S. Natesakhawat
Department of Chemical and Petroleum Engineering
University of Pittsburgh
Pittsburgh PA, 15260, USA
[d] K. Kisslinger, R. Lin, Dr. H. L. Xin
Center for Functional Nanomaterials
Brookhaven National Laboratory
Upton, NY 11973, USA
[e] Dr. E. Stavitski, Dr. K. Attenkofer, Dr. I. Waluyo
National Synchrotron Light Source II
Brookhaven National Laboratory
Upton, NY 11973, USA
[f] Y. Tang, Prof. Dr. Y. Guo
Department of Chemistry
Carnegie Mellon University
Pittsburgh, PA 15213, USA
[g] Dr. A. Roy
J. Bennett Johnston, Sr., Center for Advanced Microstructures and Devices
Louisiana State University
Baton Rouge, LA 70806, USA
** Current address: Department of Physics and Astronomy, University of California, Irvine, CA 92697, USA
*** Current address: Raith America, Inc., International Applications Center, Troy, NY 12180, USA
**** Current address: Seagate Technology, Fremont, CA 94538, USA

Supporting information for this article is given via a link at the end of the document.

## Introduction

Light olefins ($C_2$-$C_4$) are important building blocks in the chemical industry.[1] Traditionally, they are produced from steam cracking and catalytic cracking of naphtha, gas oil or light alkanes. However, these processes are extremely energy intensive with significant $CO_2$ emissions.[1a] There has also been growing interest in reducing the dependence on petroleum feedstocks for these chemicals.[1a] A promising alternative is to produce light olefins directly from syngas (CO and $H_2$), which can be derived from coal, natural gas or biomass. This direct route is more sustainable and potentially economically profitable.[1a] To this end, catalysts such as Fe- and Co- based Fischer-Tropsch to olefins (FTO) catalysts[1c, 2] and hybrid oxide-zeolites catalysts[1b] have been developed. Some catalysts have demonstrated remarkable olefins selectivity exceeding predictions from the Anderson-Schulz-Flory distribution,[1b, 2] which describes the ideal relative ratios of hydrocarbon products in a polymerization process.[3]

Iron-based catalysts have received increasing attention for FTO synthesis.[1c, 4] Despite recent advances, challenges such as poor stability and/or high methane and $CO_2$ production still persist.[1a, 1c, 4b, 5] One particular difficulty is the sintering and deactivation of catalyst nanoparticles during reaction. Strong interaction between catalyst and support can limit sintering, but it can also inhibit catalyst activity.[1c] Consequently, much attention has focused on catalyst support materials that can promote the reducibility and carburization of catalysts and minimize aggregation and fragmentation.[1c, 6] Carbon materials have been considered as promising supports.[5b, 7] For example, one of the best reported FTO catalysts is Na and S promoted iron oxide on carbon nanofibers.[1c] Compared with metal oxide supports, weak interaction between iron oxide catalyst particles and carbon nanofiber support facilitates catalyst activation while maintaining structural stability.[1c, 5b, 7b]

Herein, we report on the use of K-promoted carbon nanosheets (CNS) as supports for iron-based FTO catalysts. The CNS supports are fabricated from the carbonization of potassium citrate serving as an inexpensive carbon source with an added benefit of dispersing K promoter throughout the supports. The catalyst demonstrates high activity and stability towards $C_2$-$C_4$ light olefins and exhibits the highest reported iron time yield (FTY) values of 1790–1990 $\mu mol_{CO}/g_{Fe}$•s for ~100 h time on stream (TOS). Furthermore, the catalyst can be used repeatedly and high activity can still be achieved after 500 h of cumulative TOS. This level of catalytic performance is not achievable by simply adding K promoters to carbon and silica supports using traditional incipient wetness impregnation approaches.[1a] Various characterization results reveal that the as-deposited iron oxide catalyst nanoparticles on K-promoted CNS are more readily reduced and stabilized as metallic iron after the initial $H_2$ activation

compared with a control catalyst sample supported on carbon nanotube (CNT). The more robust formation of metallic iron on CNS results in more efficient conversion in the subsequent FTO reaction to form highly active iron carbide. Additionally, the K embedded in CNS enhances the catalyst activity and selectivity.[8] Finally, as K is a common promoter for a broad range of reactions, our approach for fabricating K-promoted CNS catalyst supports has broad utility beyond the FTO reactions demonstrated in the current study.

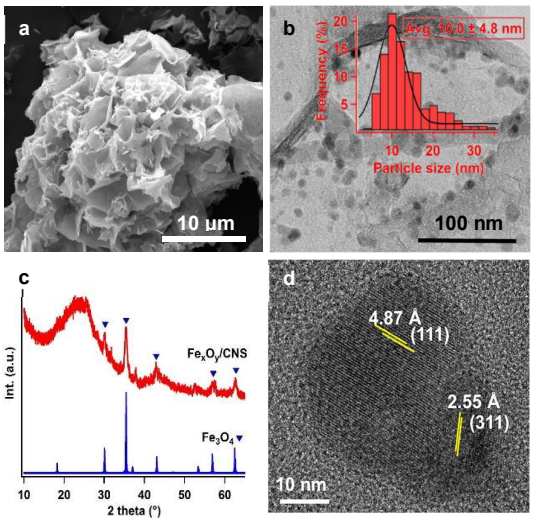


**Figure 1.** Electron microscopy and XRD characterization of $Fe_xO_y$/CNS catalyst. a) SEM and b) TEM images of the $Fe_xO_y$/CNS catalyst, (inset) size distribution of $Fe_xO_y$ nanoparticles from analysis of > 800 nanoparticles. c) XRD pattern of $Fe_xO_y$/CNS catalyst compared with the standard reference of $Fe_3O_4$ (PDF 01-076-1849). d) High resolution TEM (HRTEM) image of $Fe_xO_y$ nanoparticles showing lattice fringes consistent with the $Fe_3O_4$ phase.

## Results and Discussion

### Characterization of $Fe_xO_y$/CNS catalysts

The as-synthesized iron oxide on interconnected carbon nanosheets ($Fe_xO_y$/CNS) catalyst consists of 10.0 nm ± 4.8 nm $Fe_xO_y$ nanoparticles well dispersed on CNS with a rose-like structure (Figure 1a, b).[9] XRD indicates the main crystal phase of $Fe_xO_y$ particles is $Fe_3O_4$ (Figure 1c). The calculated size of $Fe_3O_4$ nanoparticles is 11 nm from the Scherer formula using the peak (311) at 35.4°, consistent with the TEM particle size analysis. The broad peak at 23° arises from the CNS support (Figure S1). The HRTEM images of the iron oxide nanoparticles in Figure 1d and S2 show lattice fringes of 4.9 Å and 2.6 Å corresponding to the *d* spacing of (111) and (311) planes in $Fe_3O_4$, respectively, which further confirm the XRD results.

Raman and X-ray photoelectron spectroscopy (XPS) results illustrate that the CNS are highly functionalized, with various functional groups such as carboxyl, carbonyl and C-O containing groups (Figure S3). These functional groups have been reported to contribute to catalyst performance by anchoring and stabilizing supported iron oxide nanoparticles.[1a, 4c] EDX mapping confirms the presence of evenly distributed K that was introduced during CNS synthesis by the potassium citrate precursor (Figure S4). This ubiquitous and well-dispersed K throughout the support plays a key role in the activity and selectivity of this catalyst system.

### Catalytic performance for FTO synthesis with $Fe_xO_y$/CNS catalysts

Prior to FTO reaction, $Fe_xO_y$/CNS catalysts were reduced in $H_2$ for 3 hours at 400 °C to obtain metallic iron. Good reducibility of iron oxides in iron-based FTO catalysts is essential to achieving high catalytic activity. $Fe_3O_4$ is more readily reducible compared to $Fe_2O_3$ reported in other FTO work. It can be more efficiently transformed into Fe metal during the $H_2$ activation step and subsequently to the active iron carbide phase upon syngas exposure under FTO synthesis conditions.[10] *In situ* XRD confirms the excellent reducibility of the $Fe_xO_y$/CNS system, which forms FeO and α-Fe phases in 4% $H_2$ at 300 °C, and further completely transforms to α-Fe metal at 400 °C (Figure S5). Under FTO conditions, the metallic α-Fe is then readily carburized and forms the active species $Fe_5C_2$ (see below).

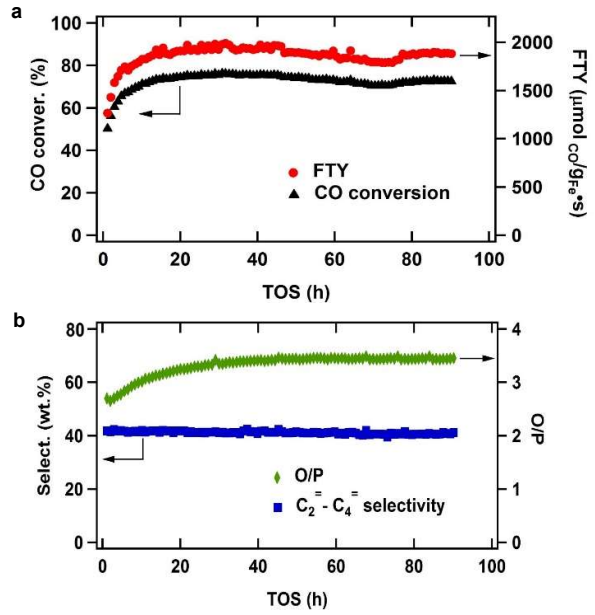


**Figure 2.** Catalytic performance of $Fe_xO_y$/CNS catalyst. a) Iron time yield (FTY) (red circles, right *y* axis), CO conversion (%, black triangles, left *y* axis), and b) light olefins selectivity (wt. %, blue squares, left *y* axis) and olefin to paraffin ratio, O/P, (green diamonds, right *y* axis) as a function of time on stream (TOS) under reaction condition of 350 °C, 20 bar, $H_2$/CO =1 and WHSV = 30,000 $cm^3$(STP)/($g_{cat}$•h).

The CO conversion, iron time yield (FTY, the number of CO molecules converted to hydrocarbons per gram of Fe per second), light olefins selectivity and olefin to paraffin ratio (O/P) are illustrated in Figure 2. In the first 10 h, the CO conversion quickly increased from 50% to 70%. This induction period corresponds to the carburization process that transforms metallic iron to catalytically active iron carbide phases. After 10 h of TOS, CO

conversion maintained its steady state at 70% until ~100 h TOS. The $Fe_xO_y$/CNS catalysts demonstrated exceedingly high FTY values between 1790–1990 $\mu mol_{CO}/g_{Fe}$•s that were far superior to other reported high performance, Fe-based carbon supported FTO or FT catalysts evaluated under similar reaction conditions. For example, FTY value of 29.8 $\mu mol_{CO}/ g_{Fe}$•s was reported for $Fe_2O_3$ on carbon nanofibers,[1c] 27.9 $\mu mol_{CO}/g_{Fe}$•s for Fe supported on N-doped carbon nanotubes,[11] while commercial Ruhrchemie catalysts produced FTYs of 22.5 $\mu mol_{CO}/g_{Fe}$•s.[12] This places our FTYs among the highest values ever achieved for iron based FTO and FT catalysts.[13] Similarly impressive FTYs were recently reported for Mg and K-promoted Fe on reduced graphene oxide catalyst, however, the activity decreased to 800–900 $\mu mol_{CO}/g_{Fe}$•s after ~ 90 h of TOS.[5b] Additionally, Figure 2b shows that the $Fe_xO_y$/CNS catalyst exhibits good and stable selectivity towards $C_2$-$C_4$ olefins with a steady-state olefin to paraffin ratio (O/P) above 3. Moreover, our reaction conditions are specifically tuned to favor short chain hydrocarbon ($C_1$-$C_5$) production and only trace and/or negligible amounts of hydrocarbons of $C_6$ and beyond were observed. We note that the $CO_2$ selectivity of our FTO catalyst is ~58 %C. In comparison, two of the best syngas to olefins synthesis catalysts have $CO_2$ selectivity of 45 %C and 42 %C.[1b, 1c] The significant $CO_2$ selectivity remains a challenge and will require further work to suppress or even eliminate $CO_2$ production. Figure S6 further shows that the same catalyst can be used repeatedly for over 500 h cumulative TOS under different reaction conditions, achieving very high activity as soon as the reaction conditions are adjusted to industrially relevant FTO conditions.

**Comparison with other FTO catalysts**

To study the role of carbon support materials, $Fe_xO_y$/CNT catalyst has been prepared and tested for FTO as a control sample. The as-received CNTs have an outer diameter of ~10 nm and length of 3-20 µm. The average size of the CNT supported $Fe_xO_y$ nanoparticles is ~ 7.3 nm (Figure 3a) and XRD indicates the oxide is also in the $Fe_3O_4$ phase (Figure S7). Despite similar characteristics between the CNT and CNS supported samples, the $Fe_xO_y$/CNS catalyst outperforms the $Fe_xO_y$/CNT in all aspects of FTO synthesis (Figure 3b, S9, Table 1). Although the CO conversion is relatively stable (~45%) for $Fe_xO_y$/CNT, it is significantly lower than that of $Fe_xO_y$/CNS (~70%), and the FTY slowly decreases from 1000 to 860 $\mu mol_{CO}/g_{Fe}$•s over 90 h TOS. Compared with the stable O/P ratio of 3.4 for the $Fe_xO_y$/CNS catalyst, the $Fe_xO_y$/CNT exhibits a substantially lower O/P ratio which also changes over time from 0.3 to 1.2 in 90 h (Figure 3b and S9).

The catalytic performance of several Fe based catalysts is summarized in Table 1. To make a more direct comparison with the K-promoted CNS system, we have prepared and evaluated the catalyst of $Fe_xO_y$/CNT promoted with 1% K (1K-$Fe_xO_y$/CNT). While the 1K-$Fe_xO_y$/CNT sample shows better olefin selectivity (54.4%) than the unpromoted $Fe_xO_y$/CNT (33.1%), its activity and stability are drastically reduced, with a CO conversion of only 4.1% at 10 h TOS and almost complete deactivation after ~18 h TOS. This finding validates that high FTO performance cannot be simply achieved by adding K onto CNTs and highlights the advantage of using CNS as a support. A standard non-supported sample, bulk Fe-Cu-K-$SiO_2$ catalyst promoted by Cu and K, achieves 52.3% CO conversion, but demonstrates poor stability after ~18 h.[1a] Finally, compared with one of the best FTO catalysts reported in the literature, $Fe_2O_3$ supported on CNF,[1c] the extraordinary 1882 $\mu mol_{CO}/g_{Fe}$•s FTY of our $Fe_xO_y$/CNS catalysts is ~60 times higher, which is also sustained with high CO conversion (72.6%) and high olefin selectivity (41.2%). All comparisons here indicate that the K-promoted $Fe_xO_y$/CNS system is one of the best performing Fe based FTO catalysts.

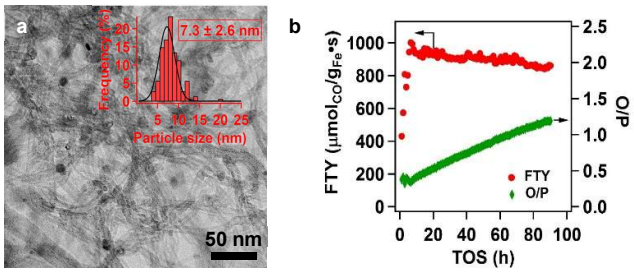


**Figure 3.** Characterization and catalytic performance of $Fe_xO_y$/CNT catalyst. a) TEM image of fresh $Fe_xO_y$/CNT catalyst, (inset) particle size distribution. b) FTY (red circles, left *y*-axis) and O/P ratio (green diamonds, right *y*-axis) of $Fe_xO_y$/CNT for FTO as a function of time on stream.

**Table 1.** Catalytic performance of $Fe_xO_y$/CNS compared with $Fe_xO_y$/CNT, 1 wt.% K promoted $Fe_xO_y$/CNT and other reference catalysts as measured by CO conversion, FTY and product selectivity under the same FTO reaction conditions (350 °C, 20 bar, $H_2$/CO=1) except $Fe_2O_3$/carbon nanofiber (CNF) (340 °C, 20 bar, $H_2$/CO=1).[1c]

| Sample | TOS (h) | CO (%) | FTY[a] | Selectivity (% wt.)[b] | | | | |
|---|---|---|---|---|---|---|---|---|
| | | | | $CH_4$ | $C_2$-$C_4$[c] | $C_2^=$-$C_4^=$[c] | $C_5^+$ | O/P |
| $Fe_xO_y$/CNS | 90 | 72.6 | 1882 | 29.9 | 53.5 | 41.2 | 16.6 | 3.35 |
| $Fe_xO_y$/CNT | 90 | 42.1 | 861 | 29.7 | 61.0 | 33.1 | 9.0 | 1.19 |
| 1K-$Fe_xO_y$/CNT | 10 | 4.1 | 89.2 | 26.3 | 64.5 | 54.4 | 9.1 | 5.36 |
| Fe-Cu-K-$SiO_2$ | 18 | 52.3 | 161 | 47.1 | 46.5 | 26.0 | 6.4 | 1.27 |
| $Fe_2O_3$/CNF[1c] | 64 | 88 | 29.8 | 13[d] | 64[d] | 52[d] | 18[d] | 6.5 |

TOS, time on stream; FTY, iron time yield; O/P, olefins to paraffins ratio.
[a] FTY is in unit of $\mu mol_{CO}/g_{Fe}$•s. [b] The selectivity is in weight percentage and excludes $CO_2$. [c] The selectivity to $C_2$-$C_4$ includes both paraffins and olefins, whereas selectivity to $C_2^=$-$C_4^=$ is specifically for olefins. [d] The selectivity for the $Fe_2O_3$/CNF catalyst is in %C, which is defined as carbon atoms in a product with respect to the total number of C atoms in the hydrocarbon mixture.[1c]

**Structure-activity correlation**

Detailed characterization of the FTO catalysts has been carried out to understand the structure-activity correlation. The $Fe_xO_y$/CNS catalysts undergo significant structural and phase changes under FTO reaction conditions (Figure 4a, b). The post-reaction iron-based nanoparticles slightly increased to an average particle size of 12.1 nm. Some larger nanoparticles (> 30 nm) were also observed (Figure 4a), indicative of some agglomeration due to sintering.

Nevertheless, both the catalytic activity and product selectivity are stable throughout the entire reaction testing process (Figure 2). Analysis of the HRTEM images indicates the post-reaction catalyst nanoparticles are composed of a $Fe_5C_2$ core with a thin amorphous iron oxide shell. The observed lattice fringes in the core are consistent with the *d* spacing of (510), (200), and (11-2) planes of $Fe_5C_2$ phase (See Figure S10a).[14] In addition, the 70° angle also agrees with the expected angle between (021) and (-11-1) planes in $Fe_5C_2$ structure (Figure 4b) as analyzed by the CrystalMaker software.[15] EDX mapping clearly illustrates the $Fe_5C_2$/amorphous iron oxide core/shell structure in the spent catalyst (Figure S10): Fe is present in both the core and shell, with C in the core and O in the shell. The same conclusion is further supported by XPS depth-profiling studies (Figure S11). As the oxide shell is gradually removed by sputtering, the embedded $Fe_5C_2$ core becomes increasingly exposed as evidenced by the growth of the peak at 708 eV associated with $Fe_5C_2$ in the XPS spectra. The amorphous iron oxide shell may result from exposing the post-reaction catalyst to air, or it may form *in situ* due to the $H_2O$ generation during FTO reaction.[16]

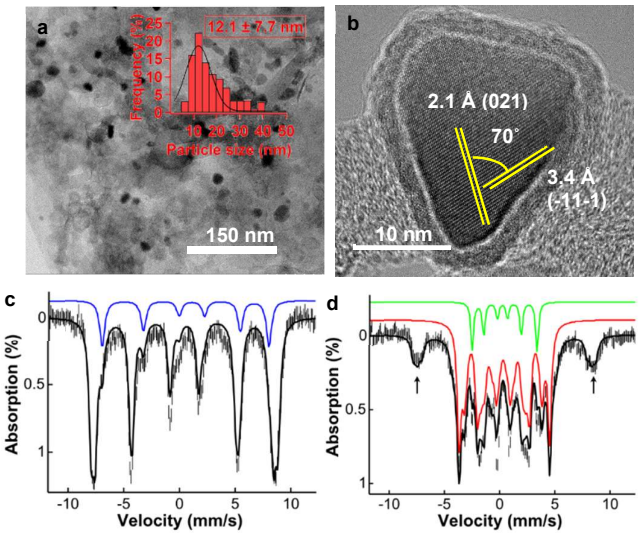


**Figure 4.** Characterization of $Fe_xO_y$/CNS catalyst after FTO reaction. a) TEM image of spent $Fe_xO_y$/CNS catalysts, (inset) particle size distribution of spent iron nanoparticles based on > 500 nanoparticles. b) HRTEM image of an isolated iron carbide/iron oxide core/shell nanoparticle with lattice spacing in the core consistent with that of $Fe_5C_2$. $^{57}$Fe Mössbauer spectra (black hashed lines) of c) the fresh $Fe_xO_y$/CNS catalyst with the overall spectral simulation (black solid line) and a magnetic subcomponent simulation representing the ferrous sites of $Fe_3O_4$ (blue solid line); d) the spent $Fe_xO_y$/CNS catalyst with the overall spectral simulation (black solid line), the spectral simulation representing χ-$Fe_5C_2$ (red solid line) and an additional iron carbide phase $Fe_xC$ (green solid line). The arrows indicate the spectral component similar to the iron oxide component in the fresh catalyst.

Mössbauer spectroscopy has been utilized to study the evolution of $Fe_xO_y$ nanoparticles during the FTO process. The Mössbauer results also quantify the types of Fe species present in the catalyst before and after reaction (Table S1). The Mössbauer spectrum of the fresh $Fe_xO_y$/CNS catalyst shows a sextet splitting pattern typically associated with magnetic iron species (Figure 4c). It suggests that $Fe_3O_4$ is the predominate phase in the fresh, unactivated, $Fe_xO_y$/CNS catalyst, consistent with the XRD and HRTEM analysis. In comparison, the Mössbauer spectrum of the spent catalyst shows significant differences (Figure 4d), which is mainly composed of χ-$Fe_5C_2$ (72% of the Fe species), with contributions from a minor $Fe_xC$ phase and a mixed oxide phase. The high χ-$Fe_5C_2$ content in the spent catalyst correlates well with its high activity and selectivity.[1c, 11, 13]

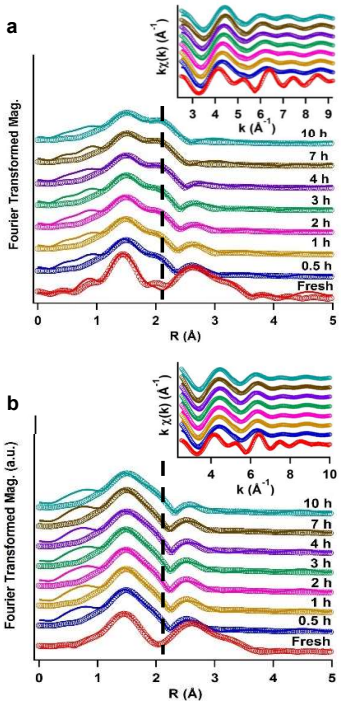


**Figure 5.** X-ray absorption spectra of $Fe_xO_y$/CNS and $Fe_xO_y$/CNT catalysts. Fourier transformed Fe K-edge EXAFS data of fresh and reacted a) $Fe_xO_y$/CNS and b) $Fe_xO_y$/CNT samples at TOS = 0 h (fresh), 0.5 h, 1 h, 2 h, 3 h, 4 h, 7 h and 10 h in $H_2$/CO (1:1) syngas at 20 bar and 350 °C. The inset shows the corresponding EXAFS spectra in *k*-space. The solid lines represent experimental data, and the circles are fitted spectra. Details of the spectra fitting are described in supplementary information. The vertical dashed lines indicate the feature of Fe-Fe coordination from $Fe_5C_2$.

X-ray absorption spectroscopy (XAS) provides important details on the transformation of iron oxide nanoparticles during FTO reactions. The evolution of the X-ray absorption near edge structure (XANES) spectra for both $Fe_xO_y$/CNS and $Fe_xO_y$/CNT catalysts at different reaction time demonstrates the conversion of iron oxide to iron carbide during FTO reaction (Figure S12), consistent with TEM, XRD and Mössbauer results shown above. Despite the similar conversion processes for the two catalyst systems, the degree of carburization of $Fe_xO_y$/CNS catalysts appears to be much more complete than that of $Fe_xO_y$/CNT

catalysts. This difference is more clearly illustrated by Fourier transformed extended X-ray absorption fine structure (EXAFS) in Figure 5. For the fresh catalysts, the first peak located between 1 and 2 Å is associated with the first Fe-O shell around the Fe absorbing core at 1.9–2.1 Å. The second peak between 2 and 3.5 Å originates from the Fe-Fe scattering of $Fe_3O_4$ at 3.0–3.5 Å (see fitting results in Table S2, S3).[8b] In the reacted catalysts, the Fe-Fe scattering from $Fe_3O_4$ in the fresh catalyst diminishes as a function of TOS. Instead, a new peak at ~ 2.0 Å appears (denoted by the vertical dashed lines in Figure 5), which is ascribed to the Fe-Fe coordination from iron carbide composition (Table S4, S5). The growth of this $Fe_5C_2$ peak is much more pronounced for $Fe_xO_y$/CNS catalysts than $Fe_xO_y$/CNT catalysts (Figure 5). These results suggest more effective carburization of iron oxide supported on CNS, leading to much improved catalytic performance for $Fe_xO_y$/CNS catalysts compared with $Fe_xO_y$/CNT catalysts (Table 1).

**Effect of catalyst supports**

As discussed in the previous section, the difference in catalyst performance for CNS and CNT supported catalysts is a result of the more complete transformation from iron oxide to iron carbide for CNS supported catalysts.[7d, 17] For quantitative comparison, the evolution of Fe-Fe coordination number for $Fe_5C_2$ from $Fe_xO_y$/CNS and $Fe_xO_y$/CNT catalysts as a function of TOS is illustrated in Figure 6a and Figure S14. The $Fe_xO_y$/CNS catalyst demonstrates higher growth rate of $Fe_5C_2$ phase than the $Fe_xO_y$/CNT catalyst. To understand the difference in carburization on different catalyst supports, the EXAFS spectrum of the $H_2$ reduced $Fe_xO_y$/CNS catalyst (Figure 6b) offers direct evidence for the presence of metallic iron,[18] whereas the $H_2$ reduced $Fe_xO_y$/CNT catalyst contains mostly oxidized Fe species (Figure 6b). Furthermore, EDX mapping of reduced $Fe_xO_y$/CNS is consistent with a core/shell structure with a metallic Fe core and an amorphous iron oxide shell presumably due to exposure to air (Figure S15). The improved reducibility of $Fe_xO_y$/CNS catalyst is also suggested by the $H_2$-TPR profiles (Figure S16).

These results suggest more robust formation of metallic Fe nanoparticles on the CNS support than on the CNT. The stabilization of metallic Fe nanoparticles by CNS subsequently leads to more effective and complete carburization upon introduction of CO under FTO conditions.[19] In contrast, for the reduced CNT supported catalyst, the less effective formation and/or stabilization of metallic iron entails that the conversion to iron carbides is hindered due to the extra barrier to push out oxygen in iron oxides.[20] These different effects of the two support materials can then explain the improved catalytic activity and selectivity for CNS supported catalysts.

One possible reason that CNS is a superior support material might be that CNS can offer an optimal interaction with the catalyst particles leading to enhanced reduction/carburization. We note that the average particle size formed on CNSs is 10±5 nm but decreases to 7±3 nm on CNTs despite using identical synthesis procedures. This may suggest a stronger interaction between the iron oxide nanoparticles and the CNT support resulting in the stabilization of smaller sized particles. This stronger interaction with the CNT support is consistent with our observation that the $Fe_xO_y$/CNT catalyst is more difficult to reduce and carburize (Figure S16).

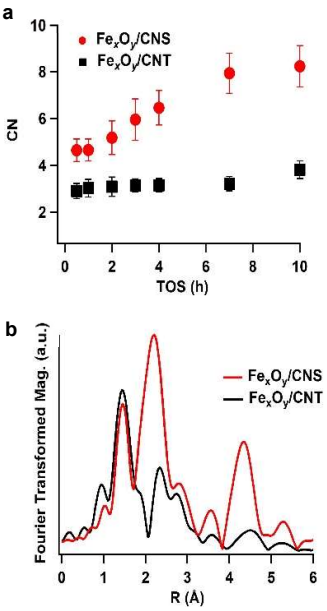


**Figure 6.** Transformation of $Fe_xO_y$/CNS and $Fe_xO_y$/CNT catalysts. a) The comparison of the evolution of the coordination number (CN) of Fe-Fe scattering from $Fe_5C_2$ composition in the $Fe_xO_y$/CNS (red circles) and $Fe_xO_y$/CNT (black squares) catalysts as a function of TOS. b) Fourier transformed Fe K-edge EXAFS spectra of $H_2$ reduced $Fe_xO_y$/CNS (red) and $H_2$ reduced $Fe_xO_y$/CNT (black) catalysts. The most significant distinction between the two spectra is the two additional peaks at 2.2 Å and 4.4 Å observed in reduced $Fe_xO_y$/CNS, which correspond to the Fe-Fe bonds from metallic iron. In contrast, the reduced $Fe_xO_y$/CNT catalyst is mostly comprised of oxidized Fe species.

Another important factor contributing to the catalytic performance of $Fe_xO_y$/CNS is the potassium contained in the CNS support. Potassium is widely used as a promoter for improving olefin selectivity and activity by facilitating the formation of Hägg carbide, improving the surface $CO/H_2$ ratio, and stabilizing active iron facets.[4c, 5b, 8a, 14b] In fact, the CNS support is specifically chosen for this work because it derives from carbonization of potassium citrate with residual K distributed evenly through the entire support (Figure S4). The $Fe_xO_y$/CNS catalyst contains 1.8 wt.% K by elemental analysis, which is consistent with surface K concentration of 1.9 wt.% estimated by XPS (Figure S17). The K should offer a promoter effect. We have also investigated the K effect in $Fe_xO_y$/CNT catalysts by adding ~ 0.1–1 wt.% K (1K-$Fe_xO_y$/CNT, Table 1); however, these K-promoted $Fe_xO_y$/CNT catalysts exhibit much lower activity and reduced stability, despite an enhancement in light olefins selectivity. This result suggests the synergistic effect of the CNS support and the inherently embedded and evenly distributed potassium leads to more effective catalyst than the ones with simple addition of K to the CNT support. Finally, we point out that K promoters are commonly used in various catalytic applications, such as ammonia

synthesis.[21] These K-promoted CNS supports should therefore have utility for a plethora of catalyst applications beyond the current demonstration for FTO reactions.

## Conclusions

We have developed a new K-promoted CNS supported $Fe_xO_y$ catalysts for FTO synthesis. The catalyst demonstrates superior catalytic activity and stability, with good olefins selectivity. Its FTY in the range of 1790–1990 $\mu mol_{CO}/g_{Fe}$•s is the highest values of reported Fe based FTO or FT catalysts, to the best of our knowledge. The catalyst is highly robust over ~100 h of TOS. Moreover, the catalyst can be reused repeatedly without degradation in catalytic performance for at least 500 h cumulative TOS. The effect of the CNS support has been investigated and compared with CNT. EXAFS studies indicate that K-promoted CNS can stabilize the metallic iron nanoparticles during $H_2$ reduction, which enhances the formation of iron carbide under FTO reaction conditions. The efficient and complete carburization of $Fe_xO_y$/CNS catalyst results in its high catalytic activity, selectivity and stability. In contrast, the CNT supported catalyst nanoparticles exhibit smaller average sizes and are more difficult to reduce, leading to less efficient transformation to catalytically active iron carbide. These observations suggest that the K-promoted CNS support offers a relatively weak but balanced interaction with the catalyst nanoparticles that enables the improved catalyst reduction and carburization while maintaining the structural integrity under reaction conditions. Future studies will focus on using operando characterization techniques as well as computational modeling to better understand the effect of K-promoted CNS catalyst support.

## Experimental Section

**Catalyst preparation**

Carbon nanosheets (CNS) were prepared by carbonization of potassium citrate, which was heated in an alumina ceramic tube under $N_2$ to 850 °C with a ramp rate of 1 ˚C/min and was held at this temperature for 1 h. This procedure is a slightly modified process using a different heating rate from that reported in the literature.[9] This recipe was chosen to not only form interconnected CNS, but also to efficiently incorporate the K promoter into the catalyst support. The product was then cleaned with 10% HCl and subsequently washed with copious amounts of water until the solution pH was neutral. The carbon nanosheets were then dried at 70 ˚C for 2 h and further dried under vacuum for 12 h.

Ammonium iron citrate was used as the Fe precursor for depositing iron oxide nanoparticle catalysts on the CNS support.[1c] Ammonium iron citrate solution (1.4 M, 333 µL) was diluted by 5 mL of water and added slowly to 500 mg of CNS until the powder was fully wet. The mixture was then allowed to dry slowly at 50 ˚C for several hours and further dried under vacuum overnight. Subsequently, the mixture was calcined at 500 ˚C for 2 h with a ramp rate of 5 ˚C/min under $N_2$ to form the $Fe_xO_y$/CNS catalyst (with nominal Fe content of 5 wt.%).

For comparison, iron-based nanoparticles supported on carbon nanotubes (CNTs) were also prepared. Ammonium iron citrate solution was mixed with multiwalled carbon nanotubes (Sigma-Aldrich) with 6-13 nm in outer diameter and 2.5-20 µm in length and the resulting mixture was processed in the same manner as described above to form $Fe_xO_y$/CNT catalyst. For K-promoted $Fe_xO_y$/CNT catalyst, $K_2CO_3$ was added to ammonium iron citrate solution for the iron oxide deposition step. Elemental analysis of the blank CNT indicates that there is a trace amount (0.01 wt.%) of Fe in the as-received CNT.

The $Fe_xO_y$/CNS catalyst were determined to contain 3.6 wt.% Fe and 1.8 wt.% K using ICP-MS. The unpromoted $Fe_xO_y$/CNT contained 4.2 wt.% Fe and no K (below the ICP-MS detection limit). The nominal 1 wt.% K-promoted $Fe_xO_y$/CNT contained 3.9 wt.% Fe and 1.2 wt. % K.

**Catalyst performance evaluation**

FTO testing was conducted in a fixed-bed reactor system (Process Integral Development Engineered & Tech.). The prepared catalysts were evaluated at 350 °C and 20 bar, which favored the production of short chain hydrocarbons. The weight hourly space velocity (WHSV) was maintained at 30,000 $cm^3$(STP)/($g_{cat}$•h). The feed gas composition was $CO/H_2/N_2$ = 45/45/10 and the total flow rate was 100 $cm^3$(STP)/min. Prior to reaction, catalyst samples (200 mg) were activated *in situ* in flowing $H_2$ (50 $cm^3$(STP)/min) at 400 °C and 1 bar for 3 h. The feed and product streams were analyzed online using an Agilent GC7890A equipped with flame ionization and thermal conductivity detectors (FID/TCD) as well as a methanizer. Separation of the compounds was performed using Ar as a carrier gas and 2 columns: molecular sieve 13X (6 ft × 1/8 in. SS, 60/80 mesh) for light gases ($H_2$, $N_2$, $CH_4$, and CO) and Hayesep Q (10 ft × 1/8 in. SS, 80/100 mesh) for $CO_2$ and $C_2$-$C_6$ hydrocarbons. CO conversion, hydrocarbon product selectivity (which excludes $CO_2$), and iron time yield (FTY) are defined as described in supplementary information.

**Catalyst characterization**

Scanning transmission electron microscopy (STEM) images were taken with a Hitachi HD-2300A dedicated scanning transmission electron microscope with a field-emission gun (FEG) and an optimal resolution of 0.204 nm. The powder catalyst sample was suspended in ethanol, spread onto a Cu grid coated with a holey carbon film (HC-Cu grid) and then dried in air. The bright-field imaging (BF), high-angle annular dark-filed (HAADF) imaging, and secondary electron imaging (SE) were carried out with a 200-kV electron probe. A Thermo Scientific Noran System SIX (NSS) energy dispersive X-ray spectroscopy (EDX) system was used to collect elemental chemistry and X-ray maps.

The atomic-resolution transmission electron microscopy (TEM) images of the catalysts were collected using an FEI Talos F200X instrument operated at 200 keV at Center for Functional

Nanomaterials at Brookhaven National Laboratory. With the aid of the ultra-bright field emitter, this instrument can image at near diffraction limit in annular dark-field STEM (ADF-STEM) mode and routinely achieve 1.4–1.5 angstrom resolution.
X-ray diffraction (XRD) measurements were carried out using a PANalytical X'pert pro X-ray diffractometer with Cu Kα radiation (λ=1.5418 Å) with a step size of 0.017° and 200 s/step in the 2θ range from 10° to 80°. The XRD was operated at 45 kV and 40 mA. The crystallite size of $Fe_3O_4$ was calculated by the Scherer equation.

$^{57}$Fe Mössbauer spectra were collected using a $^{57}$Co radiation source mounted on a velocity transducer operating under a constant acceleration mode. Velocity was calibrated with α-Fe metal. During the measurements, the samples were kept at 4.2 K in a SuperVaritemp dewar designed by Janis Research (Wilmington, MA). Mössbauer spectral simulations were performed by using the WMOSS software package (SEE Co., Edina, MN). Isomer shifts are quoted relative to α-Fe metal at 25 °C.

X-ray absorption fine structure (XAFS) experiments were carried out at the 8-ID ISS beamline at National Synchrotron Light Source II (NSLS-II) at Brookhaven National Laboratory and the XAS beamline at Center for Advanced Microstructures and Devices (CAMD) at Louisiana State University. The $Fe_xO_y$/CNS and $Fe_xO_y$/CNT catalyst samples were prepared by mixing with boron nitride (BN) (mass ratio of 1:2 due to their low Fe concentration) and were pressed into a pellet of ~1 mm in thickness. Reference samples such as $Fe_2O_3$, $Fe_3O_4$ and FeO were mixed with BN with 5 wt.% Fe in BN. For X-ray spectroscopy experiments, fresh catalysts, catalysts reduced under $H_2$ at 400 °C for 1 h, and catalysts undergoing FTO reaction conditions for different periods of time were prepared using a fixed-bed reactor under the same FTO conditions as the catalyst performance studies. All X-ray absorption measurements were conducted *ex situ* under ambient conditions. Fe K-edge XAFS data were collected in transmission mode for reference samples and in fluorescence mode for $Fe_xO_y$/CNS and $Fe_xO_y$/CNT samples. The *IFEFFIT* software package was used to analyze the XANES and EXAFS data to obtain the local structural information of iron. FEFF6 was applied to calculate single scattering paths modeled the χ(R).[22]

## Acknowledgements

We would like to thank Dr. Long Li and Dr. Kristin Bunker for their assistance with STEM experiments. This work was supported by the National Energy Technology Laboratory's ongoing research in Coal & Coal Biomass to Liquids under RES contract DE-FE0004000. This research used resources of the Center for Functional Nanomaterials, as well as beamlines 8-ID (ISS) and 23-ID-2 (IOS) of the National Synchrotron Light Source II, which are U.S. Department of Energy (DOE) Office of Science User Facilities operated for the DOE Office of Science by Brookhaven National Laboratory under Contract No. DE-SC0012704.

This project was funded by the Department of Energy, National Energy Technology Laboratory, an agency of the United States Government, through a support contract with AECOM. Neither the United States Government nor any agency thereof, nor any of their employees, nor AECOM, nor any of their employees, makes any warranty, expressed or implied, or assumes any legal liability or responsibility for the accuracy, completeness, or usefulness of any information, apparatus, product, or process disclosed, or represents that its use would not infringe privately owned rights. Reference herein to any specific commercial product, process, or service by trade name, trademark, manufacturer, or otherwise, does not necessarily constitute or imply its endorsement, recommendation, or favoring by the United States Government or any agency thereof. The views and opinions of authors expressed herein do not necessarily state or reflect those of the United States Government or any agency thereof.

## *Conflict of interest*

*The authors declare no conflict of interest.*

**Keywords:** Fischer-Tropsch • olefins • catalysis • carbon support • iron oxide

[1] a) H. M. T. Galvis, K. P. de Jong, *Acs Catal* **2013**, *3*, 2130-2149; b) F. Jiao, J. Li, X. Pan, J. Xiao, H. Li, H. Ma, M. Wei, Y. Pan, Z. Zhou, M. Li, S. Miao, J. Li, Y. Zhu, D. Xiao, T. He, J. Yang, F. Qi, Q. Fu, X. Bao, *Science* **2016**, *351*, 1065-1068; c) H. M. T. Galvis, J. H. Bitter, C. B. Khare, M. Ruitenbeek, A. I. Dugulan, K. P. de Jong, *Science* **2012**, *335*, 835-838.

[2] L. Zhong, F. Yu, Y. An, Y. Zhao, Y. Sun, Z. Li, T. Lin, Y. Lin, X. Qi, Y. Dai, L. Gu, J. Hu, S. Jin, Q. Shen, H. Wang, *Nature* **2016**, *538*, 84.

[3] I. Puskas, R. S. Hurlbut, *Catal Today* **2003**, *84*, 99-109.

[4] a) Z. Q. Yang, X. L. Pan, J. H. Wang, X. H. Bao, *Catal Today* **2012**, *186*, 121-127; b) X. Q. Chen, D. H. Deng, X. L. Pan, Y. F. Hu, X. H. Bao, *Chem Commun* **2015**, *51*, 217-220; c) Y. Cheng, J. Lin, K. Xu, H. Wang, X. Yao, Y. Pei, S. Yan, M. Qiao, B. Zong, *Acs Catal* **2016**, *6*, 389-399; d) P. Zhai, C. Xu, R. Gao, X. Liu, M. Li, W. Li, X. Fu, C. Jia, J. Xie, M. Zhao, X. Wang, Y. W. Li, Q. Zhang, X. D. Wen, D. Ma, *Angewandte Chemie International Edition* **2016**, *55*, 9902-9907; e) W. Gao, R. Gao, Y. Zhao, M. Peng, C. Song, M. Li, S. Li, J. Liu, W. Li, Y. Deng, M. Zhang, J. Xie, G. Hu, Z. Zhang, R. Long, X.-D. Wen, D. Ma, *Chem* **2018**, *4*, 2917-2928; f) D. Wang, J. Ji, B. Chen, W. Chen, G. Qian, X. Duan, X. Zhou, A. Holmen, D. Chen, J. C. Walmsley, *AIChE Journal* **2017**, *63*, 154-161; g) Z. Tian, C. Wang, Z. Si, L. Ma, L. Chen, Q. Liu, Q. Zhang, H. Huang, *Applied Catalysis A: General* **2017**, *541*, 50-59; h) B. Chen, X. Zhang, W. Chen, D. Wang, N. Song, G. Qian, X. Duan, J. Yang, D. Chen, W. Yuan, X. Zhou, *Industrial & Engineering Chemistry Research* **2018**, *57*, 11554-11560; i) D. Wang, B. Chen, X. Duan, D. Chen, X. Zhou, *J Energy Chem* **2016**, *25*, 911-916.

[5] a) A. C. J. Koeken, H. M. T. Galvis, T. Davidian, M. Ruitenbeek, K. P. de Jong, *Angew Chem Int Edit* **2012**, *51*, 7190-7193; b) Y. Cheng, J. Lin, T. J. Wu, H. Wang, S. H. Xie, Y. Pei, S. R. Yan, M. H. Qiao, B. N. Zong, *Appl Catal B-Environ* **2017**, *204*, 475-485; c) J. Barrault, C. Forquy, J. C. Menezo, R. Maurel, *Reaction Kinetics and Catalysis Letters* **1980**, *15*, 153-158.

[6] a) M. Oschatz, T. W. van Deelen, J. L. Weber, W. S. Lamme, G. Wang, B. Goderis, O. Verkinderen, A. I. Dugulan, K. P. de Jong, *Catal Sci Technol* **2016**, *6*, 8464-8473; b) B. H. Davis, in *Greener Fischer-Tropsch Processes for Fuels and Feedstocks*, Wiley-VCH Verlag GmbH & Co. KGaA, **2013**, pp. 171-191.

[7] a) U. M. Graham, A. Dozier, R. A. Khatri, M. C. Bahome, L. L. Jewell, S. D. Mhlanga, N. J. Coville, B. H. Davis, *Catal Lett* **2009**, *129*, 39-45; b) M. C. Bahome, L. L. Jewell, D. Hildebrandt, D. Glasser, N. J. Coville, *Applied Catalysis A: General* **2005**, *287*, 60-67; c) M. Casavola, J. Hermannsdörfer, N. d. Jonge, A. I. Dugulan,

K. P. d. Jong, *Advanced Functional Materials* **2015**, *25*, 5309-5319; d) V. P. Santos, T. A. Wezendonk, J. J. D. Jaen, A. I. Dugulan, M. A. Nasalevich, H. U. Islam, A. Chojecki, S. Sartipi, X. Sun, A. A. Hakeem, A. C. J. Koeken, M. Ruitenbeek, T. Davidian, G. R. Meima, G. Sankar, F. Kapteijn, M. Makkee, J. Gascon, *Nat Commun* **2015**, *6*, 6451.

[8] a) C.-F. Huo, B.-S. Wu, P. Gao, Y. Yang, Y.-W. Li, H. Jiao, *Angewandte Chemie International Edition* **2011**, *50*, 7403-7406; b) M. C. Ribeiro, G. Jacobs, R. Pendyala, B. H. Davis, D. C. Cronauer, A. J. Kropf, C. L. Marshall, *J Phys Chem C* **2011**, *115*, 4783-4792; c) D. C. Sorescu, *Surface Science* **2011**, *605*, 401-414.

[9] M. Sevilla, A. B. Fuertes, *Acs Nano* **2014**, *8*, 5069-5078.

[10] a) A. J. H. M. Kock, H. M. Fortuin, J. W. Geus, *Journal of Catalysis* **1985**, *96*, 261-275; b) S. Li, G. D. Meitzner, E. Iglesia, *The Journal of Physical Chemistry B* **2001**, *105*, 5743-5750; c) R. Warringham, A. R. McFarlane, D. A. MacLaren, P. B. Webb, R. P. Tooze, J. Taylor, R. A. Ewings, S. F. Parker, D. Lennon, *The Journal of Chemical Physics* **2015**, *143*, 174703.

[11] J. Z. Lu, L. J. Yang, B. L. Xu, Q. Wu, D. Zhang, S. J. Yuan, Y. Zhai, X. Z. Wang, Y. N. Fan, Z. Hu, *Acs Catal* **2014**, *4*, 613-621.

[12] W. P. Ma, Y. J. Ding, V. H. C. Vazquez, D. B. Bukur, *Appl Catal a-Gen* **2004**, *268*, 99-106.

[13] B. An, K. Cheng, C. Wang, Y. Wang, W. B. Lin, *Acs Catal* **2016**, *6*, 3610-3618.

[14] a) C. Yang, H. Zhao, Y. Hou, D. Ma, *J Am Chem Soc* **2012**, *134*, 15814-15821; b) V. R. R. Pendyala, U. M. Graham, G. Jacobs, H. H. Hamdeh, B. H. Davis, *Chemcatchem* **2014**, *6*, 1952-1960.

[15] J. J. Retief, *Powder Diffr* **1999**, *14*, 130-132.

[16] a) E. de Smit, F. Cinquini, A. M. Beale, O. V. Safonova, W. van Beek, P. Sautet, B. M. Weckhuysen, *J Am Chem Soc* **2010**, *132*, 14928-14941; b) M. E. Dry, *Catalysis-Science and Technology, Vol. 1*, Springer-Verlag: New York, **1981**.

[17] a) M. Casavola, J. Xie, J. D. Meeldijk, N. A. Krans, A. Goryachev, J. P. Hofmann, A. I. Dugulan, K. P. de Jong, *Acs Catal* **2017**, 5121-5128; b) B. H. Davis, *Catal Today* **2003**, *84*, 83-98; c) E. de Smit, B. M. Weckhuysen, *Chem Soc Rev* **2008**, *37*, 2758-2781.

[18] F. Wang, R. Ingalls, E. D. Crozier, *Japanese Journal of Applied Physics* **1993**, *32*, 749.

[19] K. Keyvanloo, M. K. Mardkhe, T. M. Alam, C. H. Bartholomew, B. F. Woodfield, W. C. Hecker, *Acs Catal* **2014**, *4*, 1071-1077.

[20] a) E. de Smit, I. Swart, J. F. Creemer, G. H. Hoveling, M. K. Gilles, T. Tyliszczak, P. J. Kooyman, H. W. Zandbergen, C. Morin, B. M. Weckhuysen, F. M. F. de Groot, *Nature* **2008**, *456*, 222; b) C. Beasley, M. K. Gnanamani, H. H. Hamdeh, M. Martinelli, B. H. Davis, *Catal Lett* **2018**, *148*, 1920-1928.

[21] G. Ertl, S. B. Lee, M. Weiss, *Surface Science* **1982**, *114*, 527-545.

[22] A. L. Ankudinov, B. Ravel, J. J. Rehr, S. D. Conradson, *Physical Review B* **1998**, *58*, 7565-7576.